Screening wall effects of a thin fluidized bed by near-infrared imaging

Published in:
Chemical Engineering Journal

Screening wall effects of a thin fluidized bed by near-infrared imaging

Farid Aiouache [a,*], Méabh Nic An tSaoir [a], Kuniyuki Kitagawa [b]

[a] Queen's University Belfast, School of Chemistry and Chemical Engineering, Stranmillis Road, Belfast, BT9 5AG Northern Ireland, United Kingdom
[b] Ecotopia Science Institute, Nagoya University, Chikusa-ku 464-8603, Japan

ABSTRACT

Near-infrared (NIR) imaging was used to observe water vapour flow in a gas–solid fluidized bed reactor. The technique consisted of a broadband light, an optical filter with a bandwidth centred on strong water vapour absorptions, a Vidicon NIR camera, a nozzle from which an optically active mixture of gas and water vapour was trans-illuminated by an NIR beam and collected data of transmittance were normalized to actual optical path. The procedure was applied to a thin fluidized bed reactor with a low aspect ratio of tube to particle diameters (D_t/d_p) in order to validate the wall effect on flow dynamics and mass transfer during the reduction of ceria–silica by hydrogen. High concentrations of water vapour emerged in the vicinity of the wall when the bed was operated at pseudo-static conditions but disappeared when the bed was run at minimum bubbling conditions. This result shows the capability of optical methods with affordable costs to 2D imaging opaque packed bed by using a spatially resolved probe located at the exit, which is of great benefit for *in situ* visualization of anisotropic concentrations in packed beds under industrially relevant conditions and thus for elucidation of the underlying reaction mechanism and diffusion interactions.

Crown Copyright © 2011 Published by Elsevier B.V. All rights reserved.

1. Introduction

While versatile non-intrusive techniques are available for *in situ* measurements of chemical kinetics and local velocities in gas–solid reactors, they are still not sufficiently developed to measure local concentrations inside the packed beds. Local dispersions in fixed beds are commonly measured by multiple experiments where invasive probes are placed at different locations to collect different residence time distributions [1–4]. Recent developments of spatially resolved techniques based on magnetic resonance imaging (MRI) [5–7], X-ray [8], neutron [9], and laser spectroscopy [10,11] imaging have allowed non-intrusive measurements of anisotropic flow structure, voidage, solid velocity and dispersions in liquid–solid reactors and have achieved rapid access to scalar data of chemical kinetics and associated mass transfer in a single experiment. Unfortunately, these techniques are still not sufficiently mature to be applied to gas–solid reactors due to the inherently weak signal retrieved from the gaseous phase. Wang et al. [7] reported NMR studies of gas dynamics in a particle bed fluidized by laser-polarized xenon (^{129}Xe) gas to measure gas exchange between the bubble and emulsion phases as well as the gas velocity distribution in the bed. Although these results revealed for the first time the effects of gas dynamics on rate-limited processes, they still not sufficiently mature to a variety of gases.

Nevertheless, optical techniques for two dimensional (2D) concentration measurements have taken advantage of rapid developments in tuneable lasers and 2D array detectors and have allowed experiments to be performed at high spatiotemporal resolutions. For instances, Kauranen et al. [11] have reported the measurement of a stationary gas flow with a low O_2 concentration field using a two-tone frequency modulation method, Hindle et al. [12] used fibre optics based tomography to observe spatial distributions of hydrocarbon species in a combustion chamber, Salem et al. [13] observed water breakthrough in a packed bed adsorber by a fine bandwidth laser, and Reinke et al. [14] coupled two spectroscopic techniques of Raman and laser-induced fluorescence to observe spatial profiles of stable and radical species of catalytic partial oxidation of methane between two catalytic plates accessible by lateral transparent windows. In this work, an experimental procedure based on spatially resolved near-infrared (NIR) imaging is developed. The capability of this technique is demonstrated by observing the channelling of water vapour flow subjected to the wall effect of a gas–solid fluidized bed reactor with a low aspect ratio of tube to particle diameters (D_t/d_p). The technique is non-intrusive and uses affordable tools such as a broadband NIR light, a quartz-based reactor, elements of optics commonly used in telecommunications technology, and two optical filters centred on NIR absorbing and non-absorbing wavelengths of water vapour.

Fluid flow and mass and heat transports in fixed-bed catalytic reactors of low aspect ratio are well known to be subjected to

* Corresponding author. Tel.: +44 2890974065.
E-mail addresses: f.aiouache@qub.ac.uk (F. Aiouache),
mnicantsaoir01@qub.ac.uk (M.N.A. tSaoir), kuni@esi.u-ac.jp (K. Kitagawa).

Nomenclature

C_g	water vapour concentration in the gas phase $(mol\ m^{-3})$
C_{H_2}	concentration of hydrogen in the gas-phase $(mol\ m^{-3})$
D	anisotropic dispersion coefficient $(m^2\ s^{-1})$
D_{eff}	effective diffusivity coefficient $(m^2\ s^{-1})$
d_p	particle diameter (m)
F	drag force per unit of volume $(Pa\ m^{-3})$
K	permeability of the porous media (m^2)
k	reduction rate constant (s^{-1})
L	optical path (m)
P	pressure (Pa)
P_{H_2O}	water partial pressure (Pa)
r	radial coordinate (m)
R	reactor radius (m)
r_{H_2O}	reduction rate $(mol\ m^{-3}\ g^{-1})$
T	averaged transmittance
u	superficial velocity $(m\ s^{-1})$
U_c	critical superficial velocity $(m\ s^{-1})$
U_{mb}	minimum bubbling velocity $(m\ s^{-1})$
y	mole number of oxygen vacancies per mole of reduced ceria
x	radial normalized coordinate (r/R)

Greek letters

η	fluid kinematic viscosity $(m^2\ s^{-1})$
ρ	fluid mass density $(kg\ m^{-3})$
ε	packing porosity
κ	averaged absorption coefficient through the filter bandwidth $(Pa^{-1}\ m^{-1})$
ε_{mb}	averaged porosities at minimum bubbling
ε_{mf}	averaged porosities at minimum fluidization
β	non-Darcy term (m^{-1})
Θ	surface fraction of oxygen coverage

Abbreviations

2D	two dimensional
D_t/d_p	aspect ratio of tube to particle diameters
MRI	magnetic resonance imaging
NIR	near-infrared

wall effects. Models used for large aspect ratio reactors were found not to be representative and this was more valid for fluidized bed reactors where both fluid and solid phases are under dynamic operations. For instance, pressure drop overshoots in low aspect ratio fluidized bed reactors which were found to be more pronounced have been interpreted by diverse models. Tsinontides and Jackson [15] found that the overshoot depended on the tube diameter, whereas Valverde et al. [16] who worked with much finer powders and much larger tubes, did not observe an appreciable effect. Rasanen et al. [17], who used a thin fluidized bed of 20 mm internal diameter for the drying of pharmaceutical materials, concluded that models developed in large scale industries were limited in their ability to characterize the fluidization behaviour of pharmaceutical powders. Liu et al. [18], who observed pressure drop overshoots in a thin fluidized bed, interpreted the pressure changes by the classical Ergun model extended to an additional term which translated viscous effects of the wall. In fact, pressure drops were found to be mainly driven by porosity profiles, which in low aspect ratio packed beds are not constant but change along the radial coordinates [19]. In this work, a fluidized bed with an aspect ratio of 16.7 is operated at static and minimum bubbling conditions in order to ensure

two types of radial porosity profiles. The static bed operations are performed at a pseudo-static state localized by the so-called critical superficial velocity (U_c) coinciding with maximum values of pressure drop overshoots. The fluidized bed operations are run at the minimum bubbling velocity (U_{mb}). The two types of operations will ensure no Mie-scattering from solid particles above the packed bed and two different radial porosity profiles. Compared to porosity profiles at U_c, whose values are high in the vicinity of the wall and low in the core bed, porosity profiles at U_{mb} develop opposite profiles of concentration gradients along the radial coordinate as the bubbling occurs preferentially in the central region of the bed on a time-averaged basis [20].

The work-plan is as follows: step changes in concentrations of water vapour entering a reactor filled by a non-reactive packing are performed and the outlet is visualized by 2D NIR imaging. After ensuring isothermal operation under minimum radiative cooling, a reactive packing of ceria–silica mixture is introduced and reduced by hydrogen at a superficial velocity U_c; the water vapour produced is retrieved by NIR imaging, and the operation is repeated at hydrogen velocity U_{mb}. The dynamic responses to hydrogen step changes are illustrated by images of integral data along the radial direction. The experimental data are compared to concentration profiles predicted by a 2D mass balance model that accounts for an anisotropic dispersion in the reactive bed. The reduction of ceriasilica was selected because it produces water vapour as illustrated by Eq. (1).

$$CeO_2 + yH_2 \Leftrightarrow CeO_{2-y} + yH_2O \tag{1}$$

Herein x is the mole number of oxygen vacancies per mole of reduced ceria. Interestingly, the ceria–silica mixture contains oxygen and anionic vacancies whose diffusion rates vary along the progress of the reduction [21]. At low conversions, the kinetics is dominated by surface reactions of hydrogen activation, anionic vacancies formation, and water release. At high conversions, however, a slow bulk diffusion of oxygen occurs and the wall effect on channelling should therefore vary along with the progress of the reaction.

2. Two-dimensional model of fluid dynamics and mass transfer at U_c and U_{mb} operations

A two-dimensional pseudo-homogeneous model was applied to ceria reduction by hydrogen that accounts for a material balance in the gaseous phase and on the surface of ceria–silica simultaneously. The model was applied to both the pseudo-static bed operated at U_c and the dynamic bed operated at U_{mb}. The mass balance in the gas–solid phase is expressed as:

$$\varepsilon \frac{\partial C_{g,H_2O}}{\partial t} + \nabla(-\varepsilon D \nabla C_{g,H_2O} + C_{g,H_2O}\varepsilon u) = \rho_{cat}(1-\varepsilon)r_{H_2O} \tag{2}$$

Since hydrogen was assumed to dissociate on the ceria–silica surface, the reduction rate was assumed to be of the first order towards hydrogen and the second order towards oxygen sites as reported by Gennari et al. [22].

$$r_{H_2O} = kC_{H_2}(1-\Theta_O)^2 \tag{3}$$

In the bulk of ceria–silica material, only the transport of oxygen by diffusion was assumed. Consequently, the mass balance equation is given by:

$$\frac{\partial \Theta_O}{\partial t} = -\nabla D e_{ff} \nabla \Theta_O \tag{4}$$

where ε is the packing porosity and its function of the radial direction, u is the superficial velocity, C_g is water vapour concentration in the gas phase, r_{H_2O} is the reduction rate, k is the reduction rate constant, Θ is the surface fraction of oxygen coverage, C_{H_2} is the

concentration of hydrogen in the gas-phase, D is the anisotropic dispersion coefficient whose scalar components were estimated from scalar values of the Peclet number using expressions at asymptotic limits as reported by Delgado [23] and D_{eff} is the effective diffusivity coefficient calculated from the diffusivity of water vapour in N_2 normalized by the catalyst tortuosity to porosity ratio. In minimum bubbling operations, however, the dispersion effect was not considered due to high radial mixing between phases.

The pressure drop along the bed is computed from a 2D Brinkman–Forchheimer model that accounts for porosity changes along the radial coordinate of the packing [24].

$$\nabla \varepsilon \rho u u = -\varepsilon \nabla P + \varepsilon \eta \nabla^2 u + \varepsilon F$$
$$\nabla u = 0 \tag{5}$$

The drag force per unit of volume F is expressed using Ergun's relation as:

$$F = -\frac{\eta u}{K} - \beta \rho u^2 \tag{6}$$

The permeability of the porous media K and the non-Darcy term β are calculated from Zhavoronkov's model [25].

$$K = \frac{\varepsilon^3 \, dp^2}{A(1-\varepsilon)^2}, \quad \beta = \frac{B(1-\varepsilon)}{\varepsilon^2 \, dp} \tag{7}$$

where $A = 163.35 \left(1 + \frac{1}{2(D_t/d_P)(1-\varepsilon)}\right)^2$,

$$B = 1.2 \left(1 + \frac{1}{2(D_t/d_P)(1-\varepsilon)}\right) \tag{8}$$

It should be noted that in Ergun's model [26] constants A and B correspond to 150 and 1.75, respectively. The radial porosity $\varepsilon(r)$ for the pseudo-static bed and minimum bubbling bed are calculated by using expressions of Giese et al. [24] and Xu et al. [20], respectively.

$$\varepsilon = 0.32 + 0.35 \left(\frac{2\pi x}{d_P}\right) \exp\left(-\frac{x}{1.061 d_P}\right) + 0.21 \exp\left(-\frac{x}{1.88 d_P}\right) \tag{9}$$

$$\varepsilon_{mb} = \varepsilon_{mf} \left(1 + \frac{0.895 - \varepsilon_{mf}}{(0.75 - \varepsilon_{mf})}(\varepsilon_{mb} - \varepsilon_{mf})\right)^{1 - 0.06x - 1.34x^2 + 2.65x^3 - 2.25x^4} \tag{10}$$

where P is the applied pressure, η is the fluid kinematic viscosity, ρ is the fluid mass density, x is the radial normalized coordinate (r/R), d_P is the particle diameter, r is the radial coordinate, R is the reactor radius, and ε_{mb} and ε_{mf} are averaged porosities at minimum bubbling and minimum fluidization, respectively.

3. Material and methods

3.1. Materials and apparatus

Fig. 1(a)–(c) shows the front view, top view and photograph of a quartz reactor (0.02 m I.D. and 0.5 m in height), made of fused silica and covered with a carbon-based ribbon to simulate black-body radiative heating by the side electrical heaters. Two lateral windows with an aperture of $0.01 \times 0.10 \, m^2$ were kept uncovered for side observations. An inner tube (0.008 m I.D.) which was filled with a packed bed (0.02 m height) was inserted at the centre of the reactor and whose nozzle was located at 0.01 m above the bottom base of the lateral window as shown in Fig. 1 (a). The bottom distributor was made of stainless steel wire gauze of 400 meshes. The pressure drops over the bed were measured free of pressure loss at the distributor with a differential pressure transducer (142PC02D, Sensortechnics GmbH). The packing particles

were prepared by an incipient wetness method using an aqueous solution of Ce $((NH_4)_2(NO_3)_6)$ (Wako Co.) and SiO_2 (Aerosil, $380 \, m^2/g$, SIGMA-Aldrich, Inc.) as detailed in our previous work [27]. After loading CeO_2 and SiO_2, the sample was dried at 383 K for 12 h and then calcined at 773 K for 3 h under an oxygen atmosphere ($P_{O_2} = 1.013 \times 10^4$ Pa). In order to force flow channelling, a small ratio of tube to particle diameter (D_t/d_p) was selected. Particles narrowly sieved between 0.00045 and 0.0005 m with an average diameter of approximately 0.000475 m were used. This particle size belongs to type B of the Geldart classification and allows a D_t/d_p value of 16.8.

3.2. Analysis

NIR imaging of water vapour flow in N_2 flow was conducted using a NIR Vidicon camera (Hamamatsu Photonics, C2741) with a sensing wavelength range of 400–2200 nm and positioned 0.02 m away from the quartz window as shown in Fig. 1(a). Air absorption was minimized by purging the optical path between the windows and the lenses with N_2. Two optical filters (Andover) centred at 1390 nm and 1230 nm were used for water vapour absorbing and non-absorbing regions, respectively. All images were captured by a frame-grabber card (CT3000).

4. Results and discussion

4.1. Water vapour visualization at the exit of a nozzle by NIR spectroscopy and imaging

Experiments were carried out by charging the inner reactor with water vapour in N_2 at 873 K. Water vapour was supplied from a peristaltic pump, evaporated in a preheating section, and passed through an inert packing of quartz beads as shown in Fig. 1(a). The resulting volume content of water was calculated from the N_2 volume flow rate, water mass flow rate, and temperature. The flow of water vapour blowing from the nozzle was visualized using NIR camera. Water vapour images were recorded by directing the diffuse broadband light across the exit of the well defined nozzle (0.008 mm I.D.) The light was partially absorbed depending on the water vapour concentration along the light path, passed through the filter and intercepted by NIR camera. This integral transmittance along the light path contains averaged molecular absorptions of multiple transition lines of water vapour along the filter bandwidth (20 nm), and therefore could be related to water vapour content by Beer's law:

$$\log(T_{av}) = -\kappa_{av} P_{H_2O} L \tag{11}$$

where T, L, P_{H_2O}, and κ are the averaged transmittance, optical path, water partial pressure, and averaged absorption coefficient through the filter bandwidth, respectively.

The validation test was imaging the steady-state dispersion of water vapour in N_2 using two co-current flows. Water vapour was injected from the inner empty tube at superficial velocity of 0.05 ms^{-1}, composition of 1.35 mol/m^3 whereas pure N_2 was blown in the outer tube at similar velocity. Fig. 2 shows the distribution of transmittance of water vapour blowing out of the tube at 873 K and mixing with the outer flow (N_2) and illustrates lower values of integral transmittance along the central axis due to higher optical paths than those at lateral sides. Values of transmittance in Fig. 2 at a position of 2 mm above the inner tube and normalized to actual optical path are shown in Fig. 3. In addition, transmittance profiles for concentrations of water vapour of 2.7, 1.35, 0.68 and 0.26 mol/m^3 are illustrated in Fig. 3. Lower values of transmittance are still observed in the core centre of the cross-sectional path than at the sides, whereas similar cross-sectional values of transmittance, and by inference concentrations, were expected to be
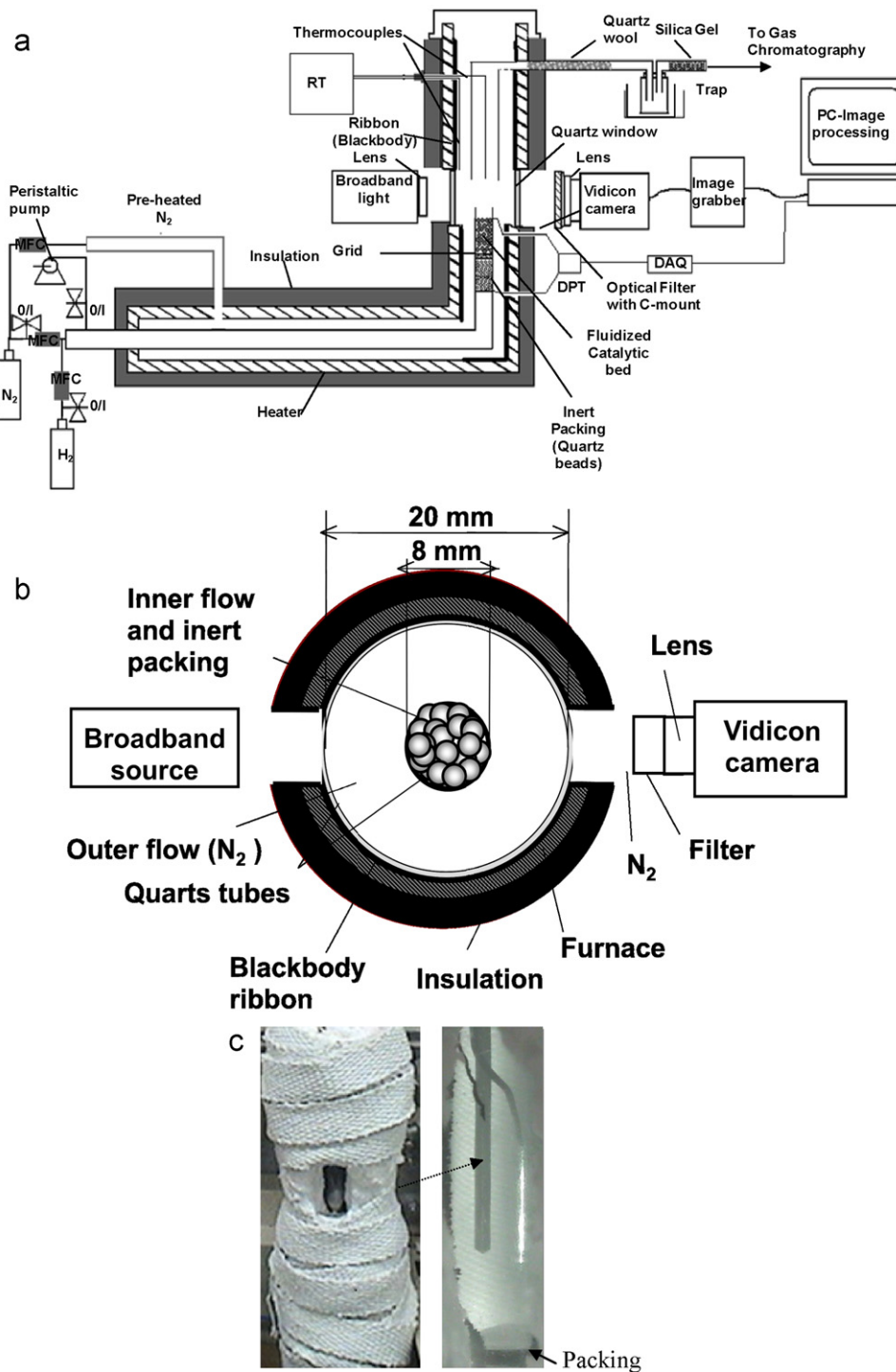
Fig. 1. Experimental setup: (a) front view; (b) top view, (c) outer tube and quartz window photographs. RT: regulator of temperature, I/O: ON/OFF valves, MFC: mass flow controller, DAQ: data acquisition, DPT: differential pressure transducer.

observed on the blowing flow from the inner tube. Such deviations in transmittance was the result of the disproportionate refraction for the light-sheet due to the circular shape of optical windows and which was indeed more pronounced towards the lateral sides of the cross-sectional flow. Profiles of deviation in transmittance along the radial coordinate and at the centre of the inner tube (no light distortion) as a function of the radial coordinate were computed for the four aforementioned concentrations as illustrated in Fig. 3. Averaged deviation profile as expressed by Eq.

(12) along with Beer's law (Eq. (11)) was taken into account for the observation of cross-sectional concentration of water vapour at the exit of the inner tube, which reproduced accurately concentration profile inside the inner tube, was used therefore for flow distribution in the static and fluidized beds in the following sections.
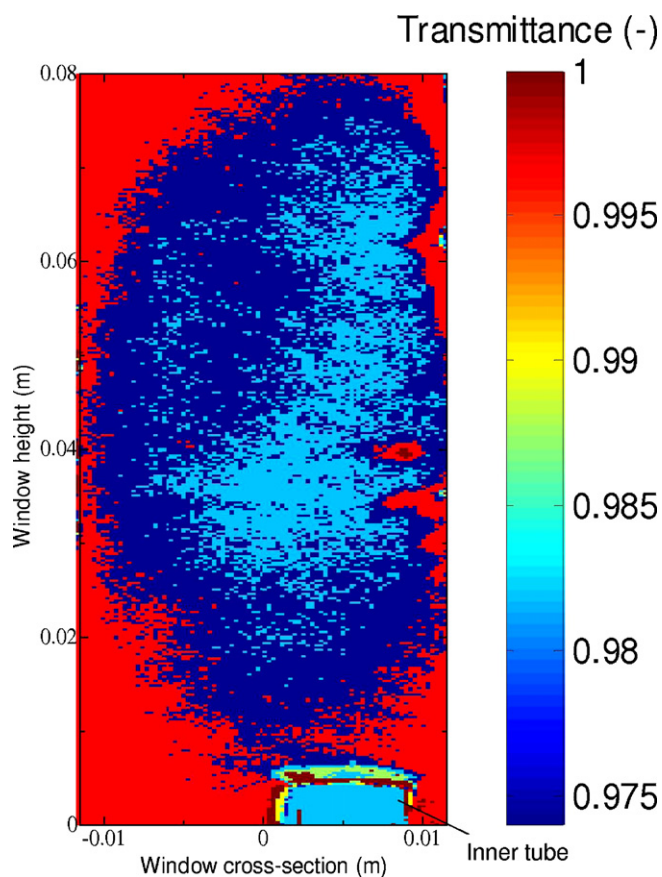
$$\Delta T = 0.031r^2 - 0.009r \tag{12}$$

Fig. 2. Integral transmittance of water vapour at the nozzle exit. Water vapour concentration: 1.35 mol/m^3 in N_2, temperature: 873 K, and pressure: 101.3 kPa, (a) inner flow ($N_2 + H_2O$) 150 ml min^{-1}, outer flow (N_2): 790 ml min^{-1}.

4.2. Screening water vapour at the exit of the fluidized bed reactor

4.2.1. Effect of gas velocity on pressure drops over the catalytic bed

A segment 0.01 m above the bottom distributor of the inner tube was filled with a pre-calcinated ceria–silica. The minimum bubbling velocity (U_{mb}) and minimum fluidization velocity (U_{mf}) were determined from a decreasing velocity run, while U_c was determined from an ascending velocity run as recommended by
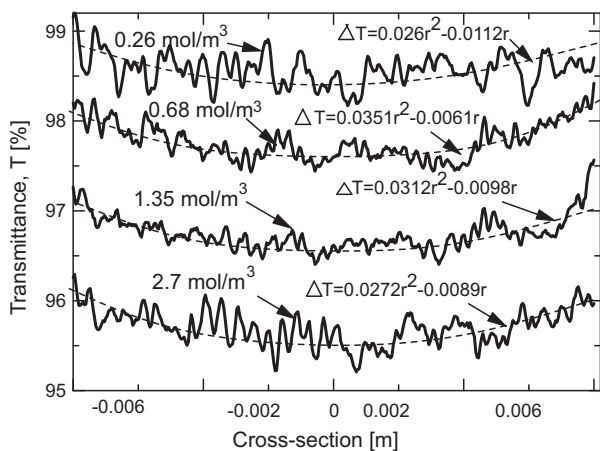

Fig. 3. Cross-sectional transmittance as a function of concentration of water vapour normalized to actual light path trans-illuminating the flow, at 2 mm above the inner tube, temperature: 873 K, and pressure: 101.3 kPa, (a) inner flow ($N_2 + H_2O$) 150 ml min^{-1}, outer flow (N_2): 790 ml min^{-1}.
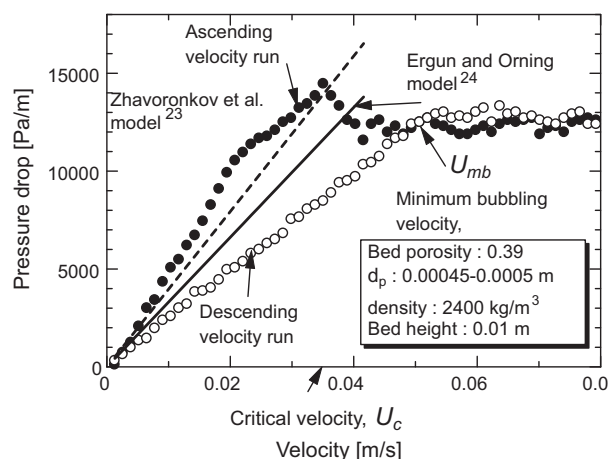

Fig. 4. Pressure drop over the fluidized catalytic bed as a function of fluid velocity.

Richardson's method [28]. Fig. 4 shows the pressure difference over the bed as a function of fluid velocity at 298 K. The pressure difference profile is similar to the profiles of group B solids of the Geldart classification. A small pressure overshoot and small oscillations were observed at a U_c value of 0.04 ms^{-1} while the U_{mb} and minimum fluidization velocity U_{mf} were found at similar values of 0.05 ms^{-1}.

The experimental data of pressure drops through the ceria–silica packing operated at both U_c and U_{mb} were compared to pressure drops obtained by Eq. (5) as shown in Fig. 4. In addition, both Ergun's model and Zhavoronkov's model are reported (continuous and dashed lines). In contrast to Ergun's model, which fitted experimental data at U_{mb} operation well, Zhavoronkov's model represented experimental data at U_c operation well. Fig. 5(a–c) show 2D simulated velocity profiles for several axial locations inside and above the bed. Local maximum velocities were five times higher in the vicinity of the wall than U_c at U_c operation, while twice higher than U_{mb} at U_{mb} operation, and thus the contribution of cross-mixing when the bed was operated at U_c was lower than at U_{mb}. It is also interesting to see that velocity profiles at the exit of the packed beds, even at short distance, do not reflect the velocity profiles inside the packing. This result illustrates the influence of the local structure on the global pressure drop at a pseudo-static and a minimum bubbling bed, which can be quite significant owing to the additional contributions of for example the shear forces and bed tortuosity to energy dissipation of the flowing gas.

4.2.2. Temperature profiles in the fluidized bed reactor

Operating the reactor at isothermal conditions is of utmost importance. Temperature profiles obtained by NIR thermography along the fluidized bed (bed emissivity was set to 0.85) and respective outer temperatures are shown in Fig. 6. The last temperatures were obtained by moving a thermocouple along the outer tube, and the velocity of N_2 was set at U_{mb}. Compared to a temperature gradient of 125 K in the outer flow, a gradient of 11 K was observed along the axial coordinate of the bed. Therefore, the additional heat from the outer flow maintained the inner reactor as close as possible to isothermal conditions and compensated for heat losses by radiative cooling compounded by the solid angles of the two optical windows.

4.2.3. Reduction of ceria in the fluidized bed at U_c and U_{mb} operations

In a single experiment, the packing bed was heated in an N_2 atmosphere at 873 K until thermal equilibrium was reached. Then, hydrogen (concentration of 1.35 mol/m^3) was charged, and averaged cross-sectional transmittance response, normalized to optical
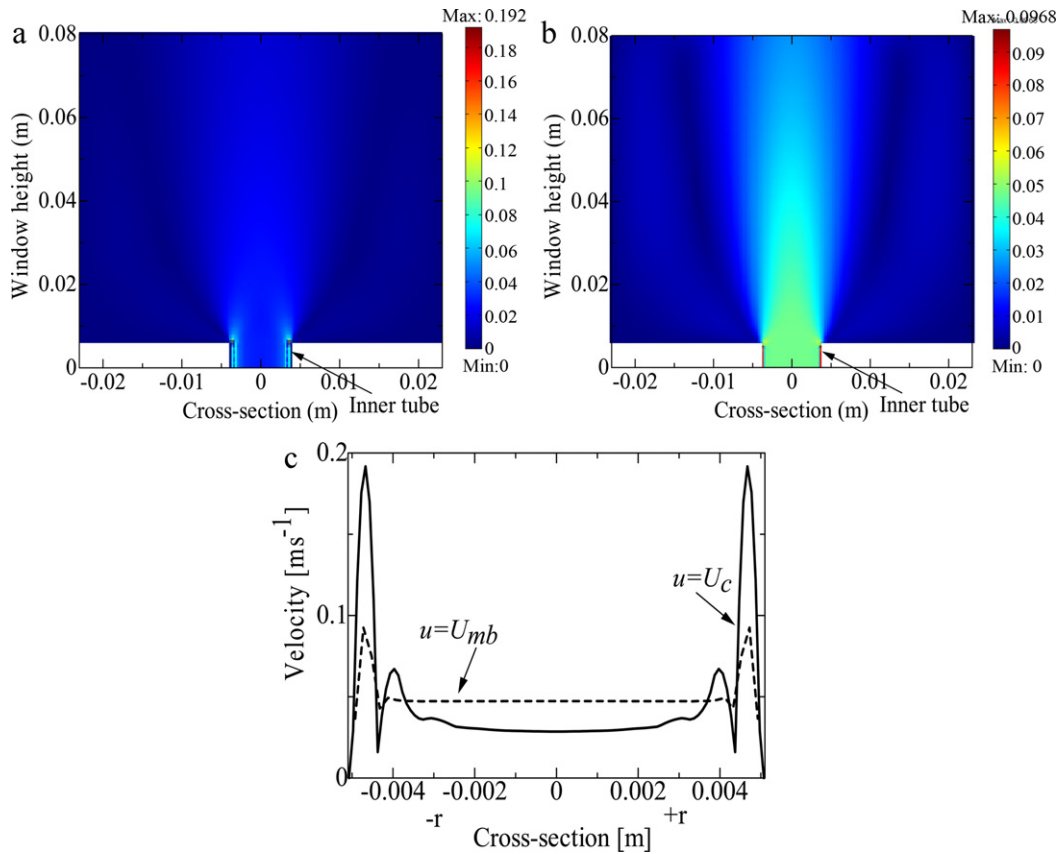
Fig. 5. Velocity distribution sat (a) pseudo static operation (b) and minimum bubbling fluidization operations, (c) cross-sectional distribution at U_c and U_{mb} operations.

path, positioned at 0.002 m above the inner tube was collected as a function of time by NIR imaging. Cross-sectional concentration profiles of water vapour inside the packed bed, obtained by Eqs. (11) and (12), as a function of the reduction time and two gas velocities U_c and U_{mb} are shown in Fig. 7(a) and (b), respectively. An initial period of fast release of water vapour lasted approximately 600 s and there was a second period which was slow but associated with a long release time. Unlike Fig. 7(b), Fig. 7(a) shows higher concentrations of water vapour in the vicinity of the wall of the inner tube than in the core centre of the bed during the period of fast release of water of 600 s. For this first period, as the reaction continued, the concentration extended from the wall to the core and covered the whole of the cross-section of the inner

reactor. This behaviour resulted from the high velocities near the wall, which led to lower residence times of hydrogen compared to the core of the bed. Flow channelling in the vicinity of the wall did occur when the bed was run at U_c. Flow channelling at the wall was not observed at slightly higher velocities such as the U_{mb} as seen in Fig. 7(b). In accordance with multiple works on porosity profiles in fluidized beds under bubbling operations, [18] the gas velocity served essentially to adjust the flow rate and volume fraction of the bubbles in the core of the bed, and accordingly induced an increase in the core porosity, while in contrast
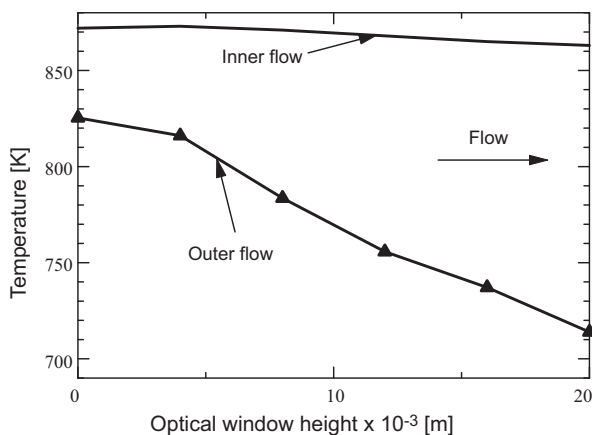

Fig. 6. Temperature profile along the fluidized bed and respective outer temperatures at U_{mb} under steady state operation, inlet feed temperature: 873 K.
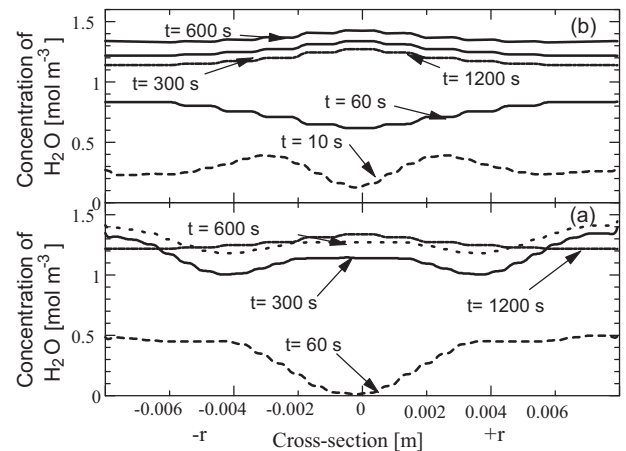

Fig. 7. Cross-sectional mole fraction reconstructed from the line of sight integral positioned at 2 mm above the nozzle during the catalytic reduction of ceria-based ceria-silica, (a) at U_c, (b) at U_{mb}, Hydrogen concentration: 1.35 mol/m^3 in N_2, temperature: 873 K, and pressure: 101.3 kPa.
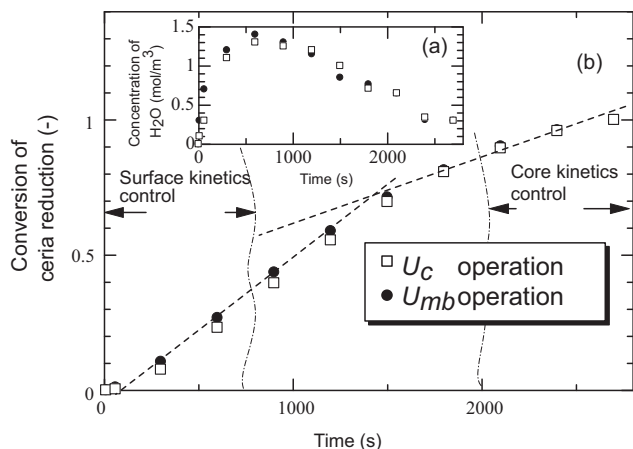
Fig. 8. Transectionally averaged concentration of water vapour (a) and conversion of catalyst reduction (b) at U_c and U_{mb} operations, hydrogen concentration: 1.35 mol/m³ in N_2, temperature: 873 K, and pressure: 101.3 kPa.

to this, the local velocity in the vicinity of wall remained nearly constant.

Fig. 8(a) and (b) shows the profiles of both transectionally averaged concentration of water vapour and respective reduction conversion at U_c and U_{mb} operations. Both figures show kinetic profiles that were slightly faster at U_{mb} operation compared with U_c operation for the first 600 s where the kinetics was under surface control. Beyond this time of reaction, the kinetics were the same at both U_{mb} and U_c operations which correspond to diffusion controlled kinetics. The apparent rate constants calculated by Eq. (3) were close to those cited in the literature [21], with values of 0.0013 and 0.0006 s⁻¹ for surface and diffusion limiting steps, respectively.

In order to confirm whether the conditions of gas flow dynamics commonly observed in fixed beds with low aspect ratios of D_t/d_p could be extended to conditions of the pseudo-static bed, the 2D mass and dynamic model expressed by Eqs. (2)–(5) was applied to the reduction of ceria-silica packing. Fig. 9(a) and (b) shows the simulated concentration profiles of water formed as a function of time and Fig. 10(a) and (b) shows 2D simulation results after 600 s at the exit of the inner tube for two experiments performed at U_c and U_{mb}, respectively. Fig. 10(a) and (b) confirms the experimental results of Fig. 10(a) and (b) in which local water vapour concentrations in the vicinity of the wall were found to be higher than at the centre of the bed at U_c operation while a negligible difference between the core and wall of the reactor was found at U_{mb} operation, which suggests that mass transfer limitations were not relevant within this first period of reduction. This period was driven by surface reduction and by the decrease in the cross-mixing in the
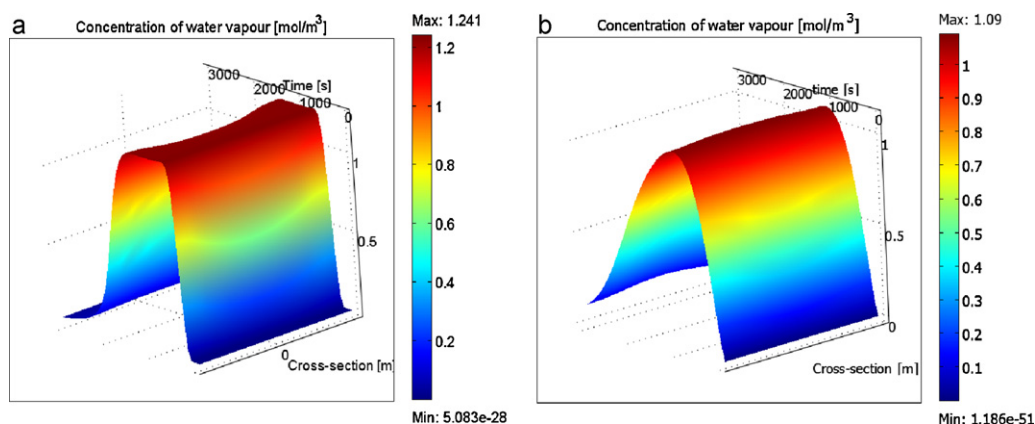

Fig. 9. Simulated results of transversal water vapour concentration at the exit of the ceria packing as a function of time: (a) U_c, (b) U_{mb}, hydrogen concentration: 1.35 mol/m³ in N_2, temperature: 873 K, and pressure: 101.3 kPa.
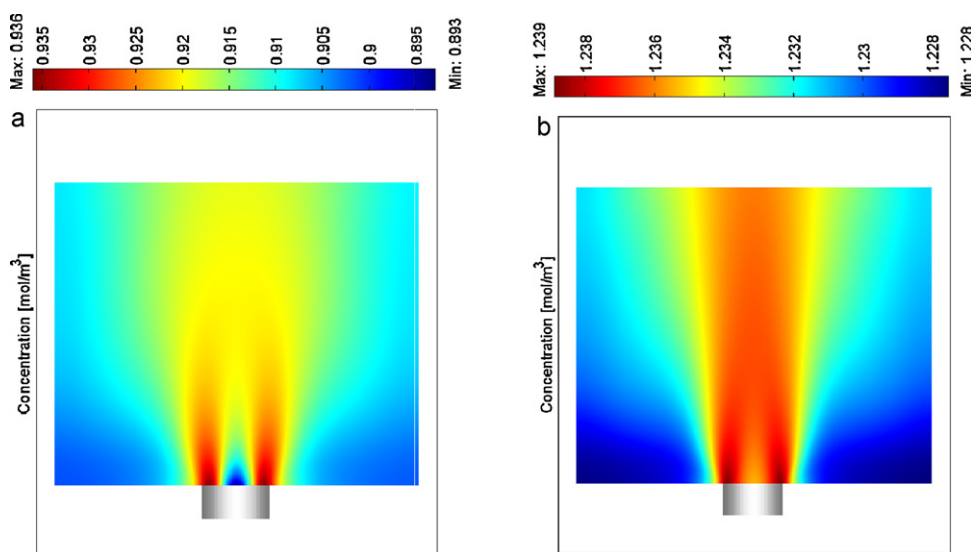

Fig. 10. 2D distribution of water vapour at the exit of the ceria–silica packing at 600 s (a) U_c, (b) U_{mb}, Hydrogen concentration: 1.35 mol/m³ in N_2, temperature: 873 K, and pressure: 101.3 kPa.

vicinity of the wall. The second period of reduction showed local concentrations of water vapour spreading from the wall to the core and the overall concentration of water vapour decreasing slowly due to bulk diffusion limitation of oxygen in the lattice of ceria as reported in the introduction on the ceria reduction mechanism. A comparison between experimental data and the simulation results shows that the time of 600 s that lasted the first period of fast reduction was reproduced by the simulation results. The experimental data show however a larger production rate of water than the simulation results during 300 s and smaller production rate after this time and up to the end of the first period of fast reduction (600 s).

5. Conclusions

This study demonstrated the value of spatially resolved NIR imaging as a promising method to screen fluid flow at the exit of a gas–solid reactor. By 2D imaging a thin fluidized bed, the proposed technique allowed existing models of thin fixed bed reactors to be extended to pseudo-static bed operations. When hydrogen was passed through the bed at U_c, it just percolated through the void spaces between the particles. When the velocity was increased beyond pseudo-static state operation to say U_{mb}, the buoyancy of the upward moving flow counterbalanced both the weight of the bed and the viscous forces in the vicinity of the wall. Thus, the fluid passed through void spaces of radial distribution, adjusted the flow rate and volume fraction of the bubbles in the core of the bed, and accordingly induced an increase in the core porosity.

The design limitations inherently associated with NIR imaging were either reduced or suppressed: (1) water vapour was used as the tracer due to its high absorption coefficient in NIR. The extension to multiple species detection such as common gases CO, CO_2 and NO_x, which are known to exhibit low absorption coefficients compared to water, is ongoing by adapting cavity enhanced absorption spectroscopy technique to a 2D design that would promote the optical path and make the technique sensitive to low compositions of low absorbing gases [29]; (2) Wall transparency and deflection were taken into account by using a highly transparent glass of small thickness. Larger thicknesses that would be convenient to higher pressure flow require the additional design of the ray geometry to be taken into account; and (3) instead of the affordable broadband light, a polarised light with large tuneability range would reach more stability, higher signal to noise ratio and detection limits of water vapour. The technique measured spatially resolved water vapour distribution along the radial coordinate of the reactor exit, and its application can therefore be of great benefit to the study of gas–solid heterogeneous processes at conditions as close as possible to those of industrial operations. The technique was extended to ceria–silica reduction, where radial profiles of water concentrations allowed the distinction between surface and bulk reduction regimes of ceria-silica packing. This design of present setup may correspond to the investigation of local catalyst deactivation by water vapour in gas–solid reactions for example in the oxidation of carbon monoxide [30], decomposition of ozone [31], low temperature water–gas-shift [32], and Fischer–Tropsch [33] but also to the control of drying of a carrier gas containing moisture in purification processes.

A present extension of the technique is under development for tomographic measurements of gaseous flow inside the reactor using NIR diffuse transmittance by a fine bandwidth laser source [29]. 3D visualization of cross-sectional profiles of water vapour and temperature but also of other species such as hydrocarbons and common gases will benefit *in situ* investigations of gaseous flows and anisotropic dispersions inside catalytic reactors. The technique revealed uneven temperature and composition maps in the core packed bed and in the vicinity of the wall due to flow maldis-tribution. In addition, the heat uptake from the packed bed and local cross-mixing were experimentally ascertained by local profiles of the water vapour composition and temperature, and thus elucidated the underlying reaction kinetics and diffusion interplays under industrially relevant conditions.

Acknowledgements

References

[1] O.M.M.-O. Coppens, Scaling-up and -down in a nature-inspired way, Industrial and Engineering Chemistry Research 14 (2005) 5011–5019.
[2] M. Nijemeisland, A.G. Dixon, E.H. Stitt, Catalyst design by CFD for heat transfer and reaction in steam reforming, Chemical Engineering Science 59 (2004) 5185–5191.
[3] M. Nijemeisland, A.G. Dixon, CFD study of fluid flow and wall heat transfer in a fixed bed of spheres, AIChE Journal 50 (2004) 5–14.
[4] H. Freund, J. Bauer, T. Zeiser, G. Emig, Detailed simulation of transport processes in fixed-beds, Industrial and Engineering Chemistry Research 44 (2005) 6423–6434.
[5] S.P. Rigby, L.F. Gladden, NMR and fractal modelling studies of transport in porous media, Chemical Engineering Science 51 (1996) 2263–2272.
[6] D.J. Holland, C.R. Muller, J.S. Dennis, L.F. Gladden, J.F. Davidson, Magnetic resonance studies of fluidization regimes, Industrial and Engineering Chemistry Research 49 (2010) 5891–5899.
[7] R. Wang, M.S. Rosen, D. Candela, R.W. Mair, R.L. Walsworth, Study of gas-fluidization dynamics with laser-polarized ^{129}Xe, Magnetic Resonance Imaging 23 (2005) 203–207.
[8] S. Roels, J. Carmeliet, Analysis of moisture flow in porous materials using microfocus X-ray radiography, International Journal of Heat and Mass Transfer 49 (2006) 4762–4772.
[9] H. Asano, T. Nakajima, N. Takenaka, T. Fujii, Visualization of the hygroscopic water distribution in an adsorbent bed by neutron radiography, Nuclear Instruments and Methods in Physics Research A 542 (2005) 241–247.
[10] C.B. Cai, Q.J. Han, L.J. Tang, L. Xu, J.H. Jiang, H.L. Wu, R.Q. Yu, Studying the uptake of aniline vapour by active alumina through in line monitoring a differential adsorption bed with near-infrared diffuse reflectance spectroscopy, Adsorption: Journal of The Internal Adsorption Society 15 (2009) 23–29.
[11] P. Kauranen, M. Hert, S. Svanberg, Tomographic imaging of fluid flows by the use of two-tone frequency-modulation spectroscopy, Optics Letters 19 (1994) 1489–1491.
[12] F. Hindle, S. Carey, K. Ozanyan, D. Winterbone, E. Clough, H. McCann, Measurement of gaseous hydrocarbon distribution by a near infra-red absorption tomography system, Journal of Electronic Imaging 10 (2001) 593–600.
[13] K. Salem, E. Tsotsas, D. Mewes, Tomographic measurement of breakthrough in a packed bed adsorber, Chemical Engineering Science 60 (2005) 517–522.
[14] M. Reinke, J. Mantzaras, R. Bombach, S. Schenker, A. Inauen, Gas phase chemistry in catalytic combustion of methane/air mixtures over platinum at pressures of 1 to 16 bars, Combustion and flame 141 (2005) 448–468.
[15] S.C. Tsinontides, R. Jackson, The mechanics of gas fluidized beds with an interval of stable fluidization, Journal of Fluid Mechanics 255 (1993) 237–274.
[16] J.M. Valverde, A. Ramos, A. Castellanos, P.K. Watson, The tensile strength of cohesive powders and its relationship to consolidation, free volume and cohesivity, Powder Technology 97 (1998) 237–245.
[17] E Rasanen, J. Rantanen, J.P. Mannermaa, J. Yliruusi, The characterization of fluidization behavior using a novel multichamber microscale fluid bed, Journal of Pharmaceutical Sciences 93 (2004) 3–8.
[18] X. Liu, G. Xu, S. Gao, Micro fluidized beds: wall effect and operability, Chemical Engineering Journal 137 (2008) 302–307.
[19] M. Winterberg, E. Tsotsas, A. Kirischke, D. Vortmeyer, A simple coherent set of efficient modelling of heat and mass transport with and without reaction in tubes filled with spheres, Chemical Engineering Science 55 (2000) 967–979.
[20] G. Xu, G. Sun, S.S. Gao, Estimating radial voidage profiles for all fluidization regimes in circulating fluidized bed risers, Powder Technology 139 (2004) 186–192.
[21] J. El-Fallah, S. Boujana, H. Dexpert, A. Kiennemann, J. Majerus, O. Touret, F. Villain, F. Normand, F. Redox, Processes on pure ceria and on Rh/CeO$_2$ catalyst monitored by X-ray absorption, Journal of Physical Chemistry 98 (1994) 5522–5533.
[22] F.C. Gennari, T. Montini, P.P. Fornasiero, J.J. Gamboa, Reduction behavior of nanoparticles of Ce$_{0.8}$Zr$_{0.2}$O$_2$ produced by different approaches, Internal Journal of Hydrogen Energy 33 (2008) 3549–3554.
[23] J.M.P.Q. Delgado, Longitudinal and transverse dispersion in porous media, Chemical Engineering Research and Design 85 (2007) 1245–1252.
[24] M. Giese, K. Rottschafer, D. Vortmeyer, Measured and modeled superficial flow profiles in packed beds with liquid flow, AIChE Journal 44 (2008) 484–490.

[25] N.M. Zhavoronkov, M.E. Aerov, N.N. Umnik, Hydraulic resistance and packing density of a layer of grains, Zhurnal Fizicheskos Khimii 23 (1949) 342–360.

[26] S. Ergun, A.A. Orning, Fluid flow through randomly packed columns and fluidized beds, Industrial and Engineering Chemistry 41 (1949) 1179–1184.

[27] F. Aiouache, O. Oyama, K. Kitagawa, Spatial near-infrared imaging of hydroxyl band coverage on ceria-based catalysts, AIChE Journal 52 (2006) 1516–1521.

[28] J.F. Richardson, Incipient fluidization and particulate systems, in: J.F. Davidson, D. Harrison (Eds.), Fluidization, Academic Press, London, 1971, pp. 25–64.

[29] M.N. An tSaoir, D. Fernandes, J. Sá, M. McMaster, K. Kitagawa, C. Hardacre, F. Aiouache, Visualization of water vapour flow in a packed bed adsorber by near infrared diffused transmittance tomography, Chemical Engineering Science, submitted.

[30] I.H. Son, The study of the deactivation of water-pretreated Pt/gamma-Al2O3 for low-temperature selective CO oxidation in hydrogen, Journal of Power Resources 124 (2003) 415–419.

[31] D.M. Yang, P.K. He, F. Dong, Effect of water vapor at room temperature on photocatalytic decomposition of gaseous ozone over Au/TiO$_2$, Chinese Journal of Catalysis 27 (2006) 1122–1126.

[32] A. Goguet, R. Burch, Y. Chen, C. Hardacre, P. Hu, R.W. Joyner, F.C. Meunier, B.S. Mun, A. Thompsett, D. Tibiletti, Deactivation mechanism of a Au/CeZrO4 catalyst during a low-temperature water gas shift reaction, Journal of Physical Chemistry C 111 (2007) 16927–16933.

[33] N.E. Tsakoumis, M. Ronning, O. Borg, E. Rytter, A. Holmen, Deactivation of cobalt based Fischer–Tropsch catalysts: a review, Catalysis Today 154 (2010) 162–182.